Volume 6 Number 3 Jul - Sep 2017

STUDENT JOURNAL OF PHYSICS

INTERNATIONAL EDITION

INDIAN ASSOCIATION OF PHYSICS TEACHERS

ISSN – 2319-3166

STUDENT JOURNAL OF PHYSICS

This is a quarterly journal published by Indian Association Of Physics Teachers. It publishes research articles contributed by Under Graduate and Post Graduate students of colleges, universities and similar teaching institutions, as principal authors.

Registered Office

Editor-in-Chief, SJP, Institute of Physics, Sainik School, Bhubaneswar, Odisha, India – 751005
(www.iopb.res.in/~sjp/)

STUDENT JOURNAL OF PHYSICS

Scope of the Journal

The journal is devoted to research carried out by students at undergraduate level. It provides a platform for the young students to explore their creativity, originality, and independence in terms of research articles which may be written in collaboration with senior scientist(s), but with a very significant contribution from the student. The articles will be judged for suitability of publication in the following two broad categories:

1. **Project based articles**
   These articles are based on research projects assigned and guided by senior scientist(s) and carried out predominantly or entirely by the student.
2. **Articles based on original ideas of student**
   These articles are originated by the student and developed by him/ her with possible help from senior advisor. Very often an undergraduate student producing original idea is unable to find a venue for its expression where it can get due attention. SJP, with its primary goal of encouraging original research at the undergraduate level provides a platform for bringing out such research works.
   It is an online journal with no cost to the author.

Since SJP is concerned with undergraduate physics education, it will occasionally also publish articles on science education written by senior physicists.

Information for Authors

- Check the accuracy of your references.
- Include the complete source information for any references cited in the abstract. (Do not cite reference numbers in the abstract.)
- Number references in text consecutively, starting with [1].

- Language: Papers should have a clear presentation written in good English. Use a spell checker.

Submission

1. Use the link "Submit" of Website to submit all files (manuscript and figures) together in the submission (either as a single .tar file or as multiple files)
2. Choose one of the Editors in the link "Submit" of Website as communicating editor while submitting your manuscript.

Preparation for Submission

Use the template available at "Submit" section of Website for preparation of the manuscript.

Re-Submission

- For re-submission, please respond to the major points of the criticism raised by the referees.
- If your paper is accepted, please check the proofs carefully.

Scope

- SJP covers all areas of applied, fundamental, and interdisciplinary physics research.

Studying the Puzzle of the Pion Nucleon Sigma Term

Christopher Kane[1]*
[1]Senior Undergraduate Student, Department of Paper and Bioprocess Engineering, SUNY ESF, Syracuse, New York, USA.

Abstract. In this paper I investigate the flavor dependence of the pion nucleon sigma term ($\sigma_{\pi N}$) for the $N_f = 2$, $N_f = 2 + 1$, and $N_f = 2 + 1 + 1$ cases, where N_f is the number of flavors. I calculate $\sigma_{\pi N}$ using the Hellmann-Feynman method which uses results of lattice quantum chromodynamics (LQCD). I use the expansion from Baryon Chiral Perturbation Theory as my nucleon mass fitting equation. I extrapolate the data to $a \to 0$, where a is the spacing of the lattice in LQCD, and apply the constraint that data must meet the condition $M_\pi L > 3.8$ to avoid finite volume effects, where M_π is the pion mass and L is the length of the lattice in LQCD. My results shed light on the recent disparity between values of $\sigma_{\pi N}$ calculated using different methods.

1. INTRODUCTION

The search for dark matter has seen a surge of interest in recent years with the hope of finding physics beyond the standard model. All current experimental searches rely on dark matter particles interacting with nucleonic matter, i.e. protons and neutrons. One leading candidate for a dark matter particle is the neutralino, which is predicted by the theory of super-symmetry [1]. In order to constrain experiments searching for the neutralino, the cross section of interaction with nucleons must be known. The pion-nucleon sigma term ($\sigma_{\pi N}$), which is a fundamental parameter in the theory of quantum chromodynamics (QCD), is used to calculate this cross section [2]. It was originally calculated by phenomenological methods but recently has been calculated using methods involving LQCD. There is a disparity between the two methods however, with $\sigma_{\pi N}$ being significantly lower using the latter method [3]. This disparity is large enough to cause concern in the dark matter community as experiments would need to be changed accordingly.

One method of calculating $\sigma_{\pi N}$ using LQCD data is called the Hellman-Feynman (HF) method. The HF theorem relates $\sigma_{\pi N}$ to the nucleon mass (M_N) dependence on the quark mass (m_q) [4]. The HF theorem can also relate $\sigma_{\pi N}$ to the nucleon mass dependence on the pion mass (M_π) as $M_\pi^2 = m_q$. From this point on, M_π and m_q will be used interchangeably with this understanding. The HF theorem is defined in Eq. 1.

$$\sigma_{\pi N} = m_q \frac{\partial}{\partial m_q} M_N(m_q) = M_\pi^2 \frac{\partial}{\partial M_\pi^2} M_N(M_\pi^2) \tag{1}$$

*Summer REU student at the Department of Physics and Astronomy, Michigan State University, East Lansing, Michigan 48823, USA. Email: cfkane@syr.edu

LQCD is used to calculate the nucleon mass from a given quark mass (quark masses need not be physical). These data points are in turn used to determine the nucleon mass dependence on the quark mass the HF theorem requires to calculate $\sigma_{\pi N}$. It does so by simulating the dynamics inside the nucleon. Nucleons are composed of three valence quarks, but from the Heisenberg Uncertainty Principle, $\Delta E \Delta t \geq \hbar 2$, we know that quark-antiquark pairs can be created and annihilated from the vacuum. Heavier quarks will be created for shorter periods of time and therefore will have a smaller effect on the internal dynamics of the nucleon. It is common in LQCD simulations to assume that only the two and three lightest flavors (up, down, strange) of quarks contribute to the dynamics and that contributions from the heavier flavors (charmed, top, and bottom) can be ignored. In this paper I present results of $\sigma_{\pi N}$ calculated from data that included the two lightest flavors ($N_f = 2$), three lightest flavors ($N_f = 2 + 1$), and four lightest flavors ($N_f = 2 + 1 + 1$) to see if the heavier quarks have a significant contribution or if they can be safely ignored in further simulations.

2. LATTICE QCD

2.1 *Overview*

QCD is the theory that describes how quarks and gluons interact via the strong force. At high energies, i.e. particle accelerators, perturbation theory can be used to perform precise calculations. At low energies however, i.e. inside a nucleon, perturbation theory fails and calculations can no longer be done. Lattice QCD is a fully non-perturbative formulation of QCD that can perform calculations at any energy [5].

LQCD works by putting spacetime on a grid as seen in Fig. 1. The quark field exists on the lattice sites and the gluon field exists on the lattice bonds connecting neighboring sites. Each lattice has three important properties, the lattice spacing a, the box length L, and the quark mass m_q. LQCD is developed such that if the following limits are taken, $\lim a \rightarrow 0$, $\lim L \rightarrow \infty$, $\lim m_q \rightarrow m_{q,physical}$, physical QCD is recovered. Because the universe we live in is continuous and infinite however, any calculations done on a lattice inherently contain systematic errors. The two major sources of systematic error are finite volume effects (L) and lattice spacing effects (a).

2.2 *Finite Volume Effects*

Finite volume effects occur when L is small compared to the wavelength of the quarks on the lattice. Instead of comparing L to the wavelength, it is usually compared to the *mass* of the quarks. To see how this can simplify quantifying finite volume effects, we look at the DeBroglie wave equation $\lambda = hp$. Because less mass implies less momentum, less mass implies a larger wavelength. So the smaller the quark mass, the larger the box must be. A useful quantity to look at in judging the magnitude of the finite volume effects is therefore the product of the pion mass and the box length $M_\pi L$. If this quantity is large enough, it is reasonable to ignore the systematic error. If it is small, steps must be taken to extrapolate the calculations to $L \rightarrow \infty$ and account for the finite volume

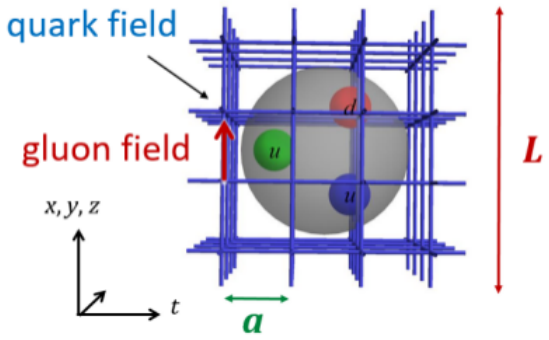

Figure 1. Image of a proton on a typical lattice in LQCD. The lattice spacing a is in green and the box length L is in red. The image is reproduced with the permission of Professor H. Lin.

effects.

2.3 *Lattice Spacing Effects*

Finite lattice spacing effects occur when a is too large to properly simulate strong force dynamics. The value of a necessary is less dependent on m_q than L. A standard value of a generally accepted to limit the size of finite lattice spacing effects is $a < 0.1$ fm. The leading corrections in the lattice spacing effects that remain are typically $O(a^2)$ [5]. As systematic errors are unique to each simulation, results can be extrapolated to $a \to 0$ by adding a term $c_j a^2$ to the fitting equation where j indicates what collaboration each data point was calculated by. The c_j terms are then treated as fitting parameters.

3. METHOD OF CALCULATION

3.1 *Applying the Hellmann-Feynman Theorem*

The HF methods requires a functional relationship between the nucleon mass and quark mass. To achieve the necessary functional relationship, I use the expansion taken from Baryon Chiral Perturbation Theory (BχPT) [6]. The first several terms of the expansion in the pion mass can be seen in Eq. 2.

$$M_N(M_\pi^2) = M_0 - 4C_1 M_\pi^2 + \frac{1}{2}\bar{\alpha} M_\pi^4 + \frac{C_1}{8\pi^2 f_\pi^2} M_\pi^4 \ln \frac{M_\pi^2}{M_0} \tag{2}$$

The terms M_0, C_1, and $\bar{\alpha}$ are low energy constants (LECs) that must be determined before calculating $\sigma_{\pi N}$. Once they are known, the HF theorem allows for a straightforward calculation of $\sigma_{\pi N}$ through a simple analytic derivative given by Eq. 3.

$$\sigma_{\pi N} = -4C_1 M_\pi^2 + \bar{\alpha} M_\pi^4 + \frac{C_1}{4\pi^2 f_\pi^2} M_\pi^4 \ln \frac{M_\pi^2}{M_0^2} + \frac{C_1}{8\pi^2 f_\pi^2} M_\pi^4 \tag{3}$$

3.2 *Determining the Low Energy Constants*

The LECs are determined by fitting Eq. 2 to the nucleon mass data generated by LQCD using varying pion masses. All sources of error are small enough compared to the error in the values of M_N and are therefore deemed negligible. Additionally, errors in M_N are assumed to be uncorrelated. To ensure that finite volume effects were negligible, points that did not satisfy $M_\pi L > 3.8$ did not enter the fit. Points were extrapolated to $a \to 0$ by including a term of the form $c_j a^2$ in the fit for each collaboration data was taken from. Three c_j terms were added in the $N_f = 2$ case and two c_j terms were added in both the $N_f = 2 + 1$ and $N_f = 2 + 1 + 1$ case. The final χ^2 function that I minimize is

$$\chi^2 = \sum_{i=1} \frac{M_N(M_\pi^2) + c_j a^2 - d_i(M_\pi^2)}{\sigma_i}, \tag{4}$$

where $d_i(M_\pi^2)$ are the LQCD data points for M_N with associated uncertainties σ_i. The common fitting parameters for all three fits include M_0, C_1, and $\bar{\alpha}$. A good fit will have χ^2/dof $\cong 1$, where dof is short for the degrees of freedom in the fit and is defined as the number of data points (d_i) minus the number of fitting parameters (i.e. M_0, C_1, $\bar{\alpha}$, c_j). Uncertainties in the fit parameters, nucleon mass, and $\sigma_{\pi N}$ were determined using the standard jackknife procedure described in [7]. All values will be given in the form mean(stdev). As an example, 7.92(13) shows that the mean value is 7.92 with an associated standard deviation is 0.13.

4. RESULTS

For the fit using $N_f = 2$ LQCD collaboration data, seven points were taken from the Mainz collaboration [8], six points were taken from the RQCD collaboration [9], and seven points were taken from the ETM collaboration [10]. The three extrapolation parameters (c_j of Eq. 4), can be found in Table 1. The c_{LQCD} and c_{RQCD} terms are consistent with zero while the c_{Mainz} term is not. This shows that the systematic error introduced in the ETM and RQCD collaborations were similar in magnitude and thus a non-zero extrapolation was necessary for the Mainz data points. For the $N_f = 2 + 1$ fit, nine points were taken from the LHP collaboration [11] and five points were taken from the NME collaboration [12]. The extrapolation parameters c_{LHP} and c_{NME} are not consistent with zero as seen in Table 1. For the $N_f = 2 + 1 + 1$ fit, fifteen points were taken from the ETM collaboration

[13] and six points were taken from the PNDME collaboration [14]. Like the $N_f = 2 + 1$ case, the extrapolation parameters c_{ETMC} and c_{PNDME} are not consistent with zero as seen in Table 1.

2*N_f = 2	c_{RQCD}	$-0.12(15)$
	c_{ETMC}	0.15(14)
	c_{Mainz}	0.55(19)
2*N_f = 2+1	c_{LHP}	0.124(9)
	c_{NME}	$-0.166(4)$
2*N_f = 2+1+1	c_{ETMC}	0.136(4)
	c_{PNDME}	$-0.042(25)$

Table 1. Extrapolation parameter values ($a \to 0$) for the N_f = 2, 2+1, 2+1+1 fits.

The fit for the $N_f = 2$ case can be seen in Fig. 2. The large χ^2/dof can be explained by analyzing the contribution of each individual data point to the total value. In this fit, three data points contributed to more than 50% of the total value. From this it is seen that using Eq. 2 as the fitting equation is appropriate, and the systematic error in the three data points in question was underestimated. The fit for the $N_f = 2 + 1$ case can be found in Fig. 3. Although the χ^2/dof is smaller than in the $N_f = 2$ case, it is still not low enough to be considered a good fit. Similar to the previous case however, three data points accounted for over 50% of the value. This leads to the same conclusion that the systematic error in those data points were underestimated. The fit for the $N_f = 2 + 1 + 1$ case can be seen in Fig. 4. The χ^2/dof is within the range to indicate a good fit. This shows that errors in all data points have appropriate errors associated with them.

N_f	M_0 [GeV]	C_1 [GeV^{-1}]	$\bar{\alpha}$ [GeV^{-3}]	$\sigma_{\pi N}$ [MeV]	$\chi^2 dof$
2	0.908(4)	$-0.55(6)$	$-5.4(1.8)$	40(4)	4.76
2+1	0.901(23)	$-0.26(18)$	11(10)	25(11)	2.04
2+1+1	0.916(18)	$-0.56(4)$	$-7.5(9)$	40(3)	1.31

Table 2. Results for BχPT fits to N_f = 2, 2+1, 2+1+1 nucleon mass data.

The values of $\sigma_{\pi N}$ for the $N_f = 2$ and $N_f = 2 + 1$ cases, seen in Table 2, agree with values produced by [6] within errorbars. Comparing the values of $\sigma_{\pi N}$ for all three cases, we see that the mean values for the $N_f = 2$ and $N_f = 2 + 1 + 1$ cases are equal with similar error bars. The mean value for the $N_f = 2 + 1$ case is significantly smaller comparatively, but has a standard deviation of 40% the mean value. Because of this large error, the value still agrees with the $N_f = 2$ case within error bars and is just over one standard deviation away from agreeing with the $N_f = 2 + 1 + 1$ case within error bars. Furthermore, comparing the values of the fitting parameters it is seen that the values of M_0 for the three cases are not statistically different. The values of C_1 and $\bar{\alpha}$ for the $N_f = 2$ and $N_f = 2 + 1 + 1$ cases are indistinguishable while the values for the $N_f = 2 + 1$ case disagree.

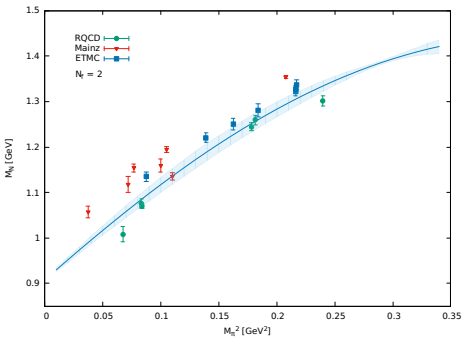

Figure 2. N_f=2 flavor fit of nucleon mass vs. pion mass squared. Data points from RQCD are in green, from Mainz are in red, and from ETMC are in blue. The shaded blue region is the uncertainty in the M_N calculations while the solid dark blue line is the mean value of M_N.

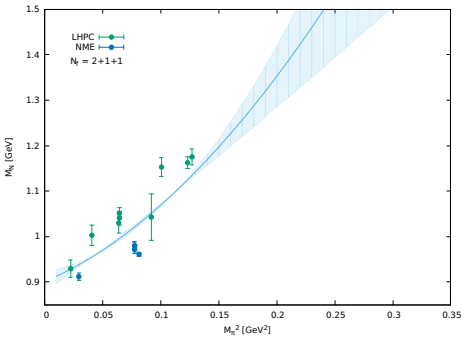

Figure 3. $N_f = 2 + 1$ flavor fit of nucleon mass vs. pion mass squared. Data points from NME are in blue and points from LHPC are in green.

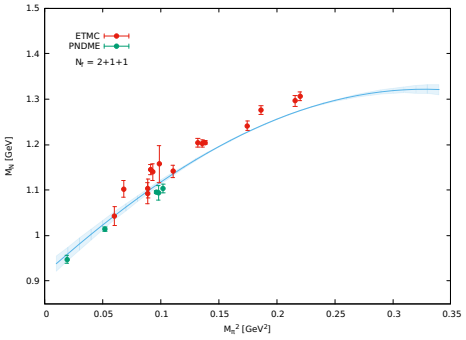

Figure 4. $N_f = 2 + 1 + 1$ flavor fit of nucleon mass vs. pion mass squared. Data points from ETMC are in red and points from PNDME are in green.

However, the error in C_1 and $\bar{\alpha}$ for the $N_f = 2 + 1$ case are, again large, with values of 70% and 90% of the mean respectively. One possibility for the large error in the $N_f = 2 + 1$ case is the small number of available data points compared to the other cases. The $N_f = 2$ and $N_f = 2 + 1 + 1$ had twenty data points that met the fit requirements while the $N_f = 2 + 1$ case had only fourteen points that met the fit requirements. Because of the large error in the parameters for the three flavor case, I cannot conclude the value of $\sigma_{\pi N}$ is statistically different from the two and four flavor case. The fits therefore show that the values of $\sigma_{\pi N}$ for the three cases are not statistically different and there is no apparent flavor dependence.

5. SUMMARY AND CONCLUSION

In this work I collected data from various collaborations generated using lattice QCD for the two flavor, three flavor, and four flavor cases. The data needed to meet the requirement that $M_\pi L > 3.8$ to assure finite volume effects could be safely ignored. Terms of the form $c_j a^2$ were added to the fitting equation to account for lattice spacing effects. This data was fitted to an expansion of the nucleon mass in terms of the pion mass developed from Baryon Chiral Perturbation Theory. Once the low energy constants were determined, I applied the Hellmann-Feynman theorem to the fitting equation in order to calculate $\sigma_{\pi N}$. Comparing the values of $\sigma_{\pi N}$ for the three cases, it is seen that they are not statistically different. This shows that after a first level analysis, $\sigma_{\pi N}$ has no significant dependence on the number of flavors included in the LQCD simulations. The inclusion of heavier quarks can therefore not account for the disparity in values calculated by phenomenological methods and LQCD methods.

6. ACKNOWLEDGEMENTS

I would like to thank Michigan State University and the NSF for the opportunity to participate in this work. I would also like to thank Professor Huey-Wen Lin for her guidance throughout the project.

References

[1] Y. Shadmi, Introduction to Supersymmetry, in Proceedings, 2014 European School of High-Energy Physics (ESHEP 2014): Garderen, The Netherlands, June 18 - July 01 2014, pp. 95123, 2016.

[2] J. Giedt, A. W. Thomas, and R. D. Young, Dark matter, the CMSSM and lattice QCD, Phys. Rev. Lett., vol. 103, p. 201802, 2009.

[3] Y.-B. Yang, A. Alexandru, T. Draper, J. Liang, and K.-F. Liu, N and strangeness sigma terms at the physical point with chiral fermions, Phys. Rev., vol. D94, no. 5, p. 054503, 2016.

[4] R. P. Feynman, Forces in molecules, Phys. Rev., vol. 56, pp. 340343, Aug 1939.

[5] R. Gupta, Introduction to lattice QCD: Course, in Probing the standard model of particle interactions. Proceedings, Summer School in Theoretical Physics, NATO Advanced Study Institute, 68th session, Les Houches, France, July 28-September 5, 1997. Pt. 1, 2, pp. 83219, 1997.

[6] L. Alvarez-Ruso, T. Ledwig, J. Martin Camalich, and M. J. Vicente-Vacas, Nucleon mass and pion-nucleon sigma term from a chiral analysis of lattice QCD data, Phys. Rev., vol. D88, no. 5, p. 054507, 2013.

[7] B. Efron, The jackknife, the bootstrap and other resampling plans. SIAM, 1982.

[8] G. von Hippel, T. D. Rae, E. Shintani, and H. Wittig, Nucleon matrix elements from lattice QCD with all-mode-averaging and a domain-decomposed solver: an exploratory study, Nucl. Phys., vol. B914, pp. 138159, 2017.

[9] G. S. Bali, S. Collins, B. Gl assle, M. G ockeler, J. Najjar, R. H. R odl, A. Sch afer, R. W. Schiel, W. S oldner, and A. Sternbeck, Nucleon isovector couplings from N f = 2 lattice QCD, Phys. Rev., vol. D91, no. 5, p. 054501, 2015.

[10] C. Alexandrou, M. Brinet, J. Carbonell, M. Constantinou, P. A. Harraud, P. Guichon, K. Jansen, T. Korzec, and M. Papinutto, Axial Nucleon form factors from lattice QCD, Phys. Rev., vol. D83, p. 045010, 2011.

[11] J. R. Green, J. W. Negele, A. V. Pochinsky, S. N. Syritsyn, M. Engelhardt, and S. Krieg, Nucleon electromagnetic form factors from lattice QCD using a nearly physical pion mass, Phys. Rev., vol. D90, p. 074507, 2014.

[12] B. Yoon et al., Isovector charges of the nucleon from 2+1-flavor QCD with clover fermions, Phys. Rev., vol. D95, no. 7, p. 074508, 2017.

[13] C. Alexandrou, V. Drach, K. Jansen, C. Kallidonis, and G. Koutsou, Baryon spectrum with N f = 2 + 1 + 1 twisted mass fermions, Phys. Rev., vol. D90, no. 7, p. 074501, 2014.

[14] G. Rajan, J. Yong-Chull, L. Huey-Wen, Y. Boram, and B. Tanmoy, Axial Vector Form Factors of the Nucleon from Lattice QCD, 2017.

One-Dimensional Chain Collisions for Different Intermediate Mass Systems

Renu Raman Sahu[1]*, **Ayush Amitabh**[2] **and Vijay A. Singh**[3†]
[1]Second Year, Int. M.Sc., School of Physical Sciences, National Institute of Science Education and Research, Jatani -752050, Odisha, India.
[2]Second Year, B.Sc., Physics Department, Patna Science College, Ashok Rajpath, Patna, Bihar-800 006, India.
[3]Centre for Excellence in Basic Sciences, Mumbai University, Kalina, Santa-Kruz East, Mumbai 400 093, India.

Abstract. It is known that one can transfer the bulk of the kinetic energy of a body to another body of smaller mass by arranging a large number of collisions with intermediate masses. In this project we explore the transfer of kinetic energy for masses arranged in arithmetic and harmonic progression. We also take into account inelastic collisions and find that there is an optimum number of intermediate masses which will ensure maximal transfer of kinetic energy. We have discovered interesting duality relations. Irrespective of the fact that the collisions are elastic or inelastic, we find that the results of arithmetic progression map onto that of the harmonic progression.

1. INTRODUCTION

Collision is one of the simplest mechanical interaction between two bodies and in the process energy and momentum are exchanged. One-dimensional collision as a means of transferring energy and ensuring velocity amplification is of interest because it provides a simple model for understanding natural phenomena where sequential collisions come into play. For example supernova explosion can be understood with the help of one-dimensional chain collision of vertically stacked masses [1]. Kerwin has explained the phenomena of super-ball collisions using an analytical method [2]. The dynamics of a queue, chain accidents in traffic, systems with narrow passage to allow for a single particle etc. can be modelled as one-dimensional chain collision systems.

The quantity of interest in studying such systems is the fraction of energy or momentum that is transferred. The exchange of kinetic energy and momentum depends mainly on the coefficient of restitution e and the ratios of colliding masses. The coefficient of restitution is a property of the colliding masses and for masses made of similar material we shall assume that it is a constant. What one can manipulate is 'mass' because one can extract a particular amount of mass from the bulk. Brilliantov and Pöschel considered viscoelastic particles where e is a function of colliding masses and their relative velocity [3]. Recently, Ricardo and Lee showed that the maximum transfer of

*renu.sahu@niser.ac.in
†physics.sutra@gmail.com

kinetic energy takes place if the intermediate masses are geometric means of final and initial mass [4]. They have also considered the case of inelastic collision with fixed coefficient of restitution e.

In our work, we take two different intermediate mass systems and compare the numerical values of kinetic energy and velocity transfer ratios for a given value of initial and final mass. Unlike Ricardo and Lee, we take masses in arithmetic and harmonic progression. We consider the general case of inelastic collision.

2. BASIC EQUATIONS

We assume that the two colliding masses are spheres placed on the x- axis in such a way that the distance between their centres is greater than the sum of their radii. Let a mass M moving with velocity V, collide with a mass m which was intially at rest and due to which it's velocity changes to V' while the mass m gains a velocity v. This is shown in Fig. 1.

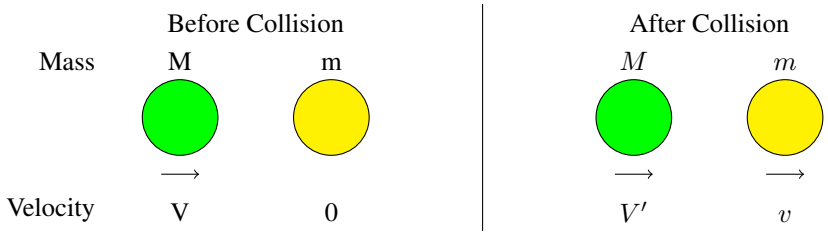

Figure 1. Collision of two masses

We define the velocity transfer ratio r_v as

$$r_v = \frac{v}{V}$$

Similarly kinetic energy transfer ratio is defined as

$$r_K = \frac{\frac{1}{2}mv^2}{\frac{1}{2}MV^2}$$

Since the momentum is conserved we have

$$MV = MV' + mv \tag{1}$$

The coefficient of restitution is

$$e = (v - V')/V \tag{2}$$

Using eqns. (1) and (2) we get the expression for velocity transfer ratio

$$r_v = \frac{(e+1)M}{(M+m)} \tag{3}$$

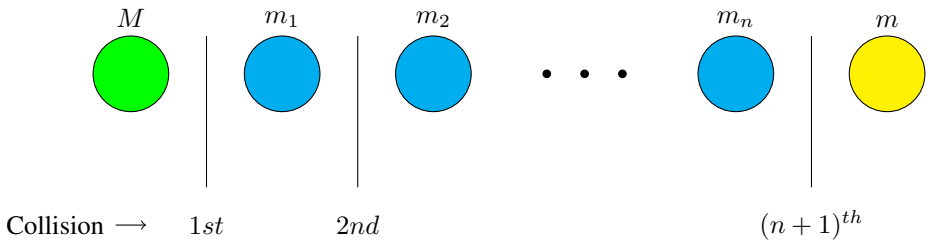

Figure 2. There are n intermediate masses between M and m and $(n+1)$ colisions.

Using eqn. (3) in the definition of kinetic energy transfer ratio for inelastic collision we get

$$r_K = \frac{(e+1)^2 Mm}{(M+m)^2} \tag{4}$$

Now consider the situation with n intermediate masses $m_1, m_2, m_3 \ldots m_n$ between M and m. For the transfer of kinetic energy from M to m there has to be $n+1$ collisions. Initially the sphere of mass M was moving with velocity V towards the above described assembly of set of stationary masses. After the first collision let the velocity of M be V' and that of m_1 be v_1. Then after the second collision between m_1 and m_2 the velocity of m_1 becomes v_1' and m_2 gains a velocity v_2. Generalising the notation, the i^{th} collision is between m_{i-1} and m_i. Just after $(i-1)^{th}$ collision m_{i-1} gets a velocity v_{i-1} and after the i^{th} collision it becomes v_{i-1}'. The velocity of mass m_i is v_i after i^{th} collision. Let the velocity transfer ratio and kinetic energy transfer ratio at i^{th} collision be denoted by r_{vi} and r_{Ki} respectively.

It can be shown that the velocity transfer ratio for i^{th} collision is

$$r_{vi} = \frac{v_i}{v_{i-1}} = \frac{(e+1)m_{i-1}}{m_{i-1}+m_i} \tag{5}$$

and the kinetic energy transfer ratio is

$$r_{Ki} = \frac{\frac{1}{2}m_i v_i^2}{\frac{1}{2}m_{i-1}v_{i-1}^2} = \frac{(e+1)^2 m_{i-1}m_i}{(m_{i-1}+m_i)^2} \tag{6}$$

Given the initial velocity of mass M we want to find r_v and r_K. From the definition of velocity transfer ratio

$$r_v = \frac{v}{V}$$

Multiplying and dividing with v_i where $i = 1, 2, 3 \ldots n$ we get

$$\begin{aligned} r_v &= \frac{v_1}{V}\frac{v_2}{v_1}\cdots\frac{v_n}{v_{n-1}}\frac{v}{v_n} \\ &= \prod_{i=1}^{n+1} r_{vi} \end{aligned}$$

Similarly

$$r_K = \prod_{i=1}^{n+1} r_{Ki} \tag{7}$$

Next we consider two intermediate mass systems, arithmetic and harmonic.

3. INTERMEDIATE MASS SYSTEMS

3.1 *Intermediate Masses in Arithmetic Progression*

In this case the intermediate masses m_i are such that $M > m_1 > m_2 \ldots m_n > m$ and the magnitude of difference of any two consecutive masses is a constant for the system. That is

$$M - m_1 = m_{i-1} - m_i = m_n - m$$

where $i = 2, 3 \ldots n$ Let the common difference be denoted by d.

$$d = \frac{M - m}{n + 1} \tag{8}$$

Mass of i^{th} intermediate sphere is $m_i = M - id$. Substituting the value of d from eqn. (8) we get

$$m_i = \frac{(n + 1 - i)M + im}{n + 1} \tag{9}$$

Similarly

$$m_{i-1} = \frac{(n + 2 - i)M + (i - 1)m}{n + 1}$$

Using eqns. (5), (7) and (9), the velocity transfer ratio is

$$r_v = \prod_{i=1}^{n+1} \frac{(e + 1)[(n + 2 - i)M + (i - 1)m]}{[2(n - i) + 3]M + (2i - 1)m} \tag{10}$$

The momentum transfer ratio r_{pi} for the i^{th} collision is obtained by multiplying the mass ratio m_i/m_{i-1} with r_{vi}. So, the momentum transfer ratio is

$$r_p = \prod_{i=1}^{n+1} \left(\frac{(e + 1)[(n + 1 - i)M + im]}{[2(n - i) + 3]M + (2i - 1)m} \right) \tag{11}$$

Similarly, using eqns. (6), (7) and (9), the kinetic energy transfer ratio is

n	$e = 1$	$e = 0.99$	$e = 0.95$	$e = 0.90$
0	0.7462	0.7388	0.7094	0.6735
1	0.8508	0.8361	0.7688	0.6929
2	0.8953	0.8705	0.7691	0.6581
3	0.9196	0.8835	0.7510	0.6101
4	0.9348	0.8891	0.7257	0.5597
5	0.9453	0.8901	0.6976	0.5108
6	0.9528	0.8882	0.6685	0.4647
7	0.9585	0.8847	0.6393	0.4219
8	0.9630	0.8799	0.6106	0.3825
9	0.9666	0.8784	0.5826	0.3465

Table 1. The energy transfer r_K for varying number (n) of intermediate masses is depicted in this table. Here the mass ratio $x = m/M = 0.33$. See text for discussion.

x	$e = 1$		$e = 0.99$		$e = 0.95$		$e = 0.90$	
	n_{opt}	r_K	n_{opt}	r_K	n_{opt}	r_K	n_{opt}	r_K
0.10	∞	1	13	0.7539	5	0.5394	3	0.4261
0.33	∞	1	5	0.8901	2	0.7691	1	0.6929
0.50	∞	1	3	0.9313	1	0.8498	0	0.8022

Table 2. Optimum number of intermediate masses (n_{opt}) and corresponding energy transfer (r_K) for various mass ratios (x) and coefficient of restitution (e).

$$r_K = \prod_{i=1}^{n+1} \frac{(e+1)^2[(n+1-i)M + im][(n+2-i)M + (i-1)m]}{[(2(n-i)+3)M + (2i-1)m]^2} \tag{12}$$

The above expression for kinetic energy transfer is displayed for $x = 0.33$ in Table 1. For nearly elastic collision (e.g. e = 0.99), the optimum number of collisions is $n_{opt} = 5$. As the collision becomes increasingly inelastic, n_{opt} shifts to lower values. In fact for $e = 0.9$, n_{opt} is 1. For realistic scenarios, the exercise of introducing intermediate masses is counter-productive.

In Table 2 we display the optimum number of collisions for varying mass ratios. Even for an almost elastic collision ($e = 0.99$), the kinetic energy transfer is sub-optimal varying from 93% to 75%. For a realistic case like $e = 0.90$ we find that the exercise of introducing intermediate masses is not beneficial.

3.2 *Intermediate Masses in Harmonic Progression*

For the intermediate masses to be the harmonic means of M and m, their reciprocals have to be the arithmetic means of $1/M$ and $1/m$. Let us denote the common difference by d'. So,

$$d' = \left(\frac{\frac{1}{m} - \frac{1}{M}}{n+1} \right) \tag{13}$$

The reciprocal of i^{th} mass is

$$\frac{1}{m_i} = \frac{1}{M} + id'$$

On simplifying further we get

$$m_i = \frac{Mm(n+1)}{(n+1-i)m + iM} \tag{14}$$

Similarly the mass of $(i-1)^{th}$ sphere will be

$$m_{i-1} = \frac{Mm(n+1)}{(n+2-i)m + (i-1)M}$$

Using eqns. (5), (7) and (14) the velocity transfer ratio is

$$r_v = \prod_{i=1}^{n+1} \left(\frac{(e+1)[(n+1-i)m + iM]}{[2(n-i)+3]m + (2i-1)M} \right) \tag{15}$$

The momentum transfer ratio in this case is

$$r_p = \prod_{i=1}^{n+1} \frac{(e+1)[(n+2-i)m + (i-1)M]}{[2(n-i)+3]m + (2i-1)M} \tag{16}$$

Now, using eqns. (6), (7) and (14) the kinetic energy transfer ratio is

$$r_K = \prod_{i=1}^{n+1} \left(\frac{(e+1)^2[(n+2-i)m + (i-1)M][(n+1-i)m + iM]}{[(2(n-i)+3)m + (2i-1)M]^2} \right) \tag{17}$$

3.3 *Symmetry*

A numerical exercise for the mass ratio m/M=0.33 in the harmonic case yields results identical to the arithmetic case of Table 2. This is not surprising since an interesting symmetry relation can be discerned by examining the relevant expressions. For a system with n intermediate masses, it is seen that the velocity transfer ratio in the $(n+2-i)^{th}$ collision for the arithmetic mean system is the same as that in i^{th} collision of the harmonic mean system. Replacing i by $(n+2-i)$ we get the self-same expression for the velocity transfer ratio of i^{th} collision in harmonic mean system.

$$(r_{vi})_{AP} = \frac{(e+1)[(n+2-i)M + (i-1)m]}{[2(n-i)+3]M + (2i-1)m} \tag{18}$$

Replacing $i \to n+2-i$ in eqn. 18

$$\left(r_{v(n+2-i)}\right)_{AP} = \frac{(e+1)[(n+2-(n+2-i))M + ((n+2-i)-1)m]}{[2(n-(n+2-i))+3]M + (2(n+2-i)-1)m}$$

This simplifies and we get

$$\left(r_{v(n+2-i)}\right)_{AP} = \frac{(e+1)[iM + (n+1-i)m]}{[(2i-1)M + (2(n-i)+3)m]} \qquad = (r_{vi})_{HP} \tag{19}$$

Now it immediately follows that the kinetic energy transfer ratio will be same for $(n+2-i)^{th}$ collision in arithmetic mean system and i^{th} collision in harmonic mean system.

$$\left(r_{K(n+2-i)}\right)_{AP} = (r_{Ki})_{HP} \tag{20}$$

It is easy to see that the final velocity transfer ratio and kinetic energy transfer ratio will be same for both progressions.

Consider the expression for momentum transfer for i^{th} collision in the harmonic case.

$$(r_{pi})_{HP} = \frac{(e+1)[(n+2-i)m + (i-1)M]}{[2(n-i)+3]m + (2i-1)M} \tag{21}$$

An interesting relation exists. If we switch the masses $M \leftrightarrow m$ for the velocity gain (eqn. (18)), we obtain the corresponding momentum gain for the harmonic case (eqn. (21)). The reverse is also true.

4. CONCLUSION

We began by discussing that full transfer of kinetic energy from one body to another is not possible, if their masses are unequal. However, a judicious introduction of intermediate masses may ensure optimum transfer of kinetic energy. We have taken two different intermediate mass systems, arithmetic and harmonic. An interesting duality relation between arithmetic and harmonic was observed (section 3.3). We find that for realistic scenarios the exercise of introducing intermediate masses yields limited benefit. This scheme is a paradigm for similar exercises, such as impedance matching in electrical circuits. We hope to explore such connections in the near future.

5. ACKNOWLEDGEMENTS

One of us (VAS) acknowledges support from the Raja Ramanna Fellowship by the DAE. We thank the NIUS Physics Programme, HBCSE-TIFR, Mumbai-400088 for valuable support.

References

[1] Mellen W R, 1968, Superball rebound projectiles, Am. J. Phys. pp–845

[2] Kerwin J D, 1972, Velocity Momentum and Energy Transmissions in Chain Collisions, Am. J. Phys 1152–7

[3] Thorsten Pöschel and Nikolai V. Brilliantov, 2001, Extremal collision sequences of particles on a line: Optimal transmission of kinetic energy, PhysRevE.63.021505 1–9

[4] Bernard Ricardo and Paul Lee, 2015, Maximizing Kinetic Energy transfer in one-dimensional many-body collisions, Eur. J. Phys. 36 205013

The Jaggery (*Gud*) Mounds of Bijnor

Lakshya P. S. Kaura[1] **and Praveen Pathak**[2*]
[1]Class 12, Delhi Public School, Sector 19, Faridabad, Haryana, India 121002
[2]Homi Bhabha Center for Science Education,
Tata Institute of Fundamental Research, Mankhurd, Mumbai, India 400088

Abstract. Jaggery (unrefined sugar) is locally made during the sugarcane harvesting season in Bijnor, a major sugarcan growing area in India. As the hot semisolid heaps of jaggery are poured on the workfloor they acquire predictable shapes. We analyse the formation of one such shape employing elementary hydrodynamics. We obtain an interesting relation between the shear stress and the height of the jaggery mound. Using the equation of continuity and plausible assumptions we attempt to explain why the shape of the mound remains invariant. A similar approach can be used to understand a variety of shapes from porous sugar candy to glaciers.

1. INTRODUCTION

Bijnor in western Uttar Pradesh (UP) is arguably the jaggery capital of India. On the bus route from Moradabad to Meerut one can catch sight of huge mounds of jaggery (called *gur* or *gud* in Hindi and *panella* in Cental and South America) during the peak sugarcane harvesting season as one passes by this town. Indeed, the production of jaggery is a cottage industry in almost all areas of the world where sugarcane is grown in abundance.

Sugarcane is crushed and its juice is boiled and evaporated in large shallow pans. Often lime or a chemical is added so that the impurities rise to the top in a frothy mixture and are removed. The semi-solid mixture is yellow to dark brown in colour. It is scooped using small buckets and poured on to a clean floor. The shape acquired by these jaggery mounds are varied but at times one can see the shape as shown in Fig. 1. Two wooden planks or metal sheets are placed at two ends (y = 0 and $2L$) and the hot jaggery is poured close to the meridian defined by the y axis at a more or less steady rate. The hot viscous jaggery spreads symmetrically from the centre to the sides ($x = -L/2$ to $x = L/2$). In this article we try to understand the profile of this mound using our knowledge of elementary fluid mechanics.

2. THE PROFILE OF THE MOUND

We can consider the jaggery mound to be an incompressible viscous fluid system. Over short time scales we take the height profile $H(x, y)$ to be fixed and independent of y. In this paper we attempt

*praveen2600@gmail.com

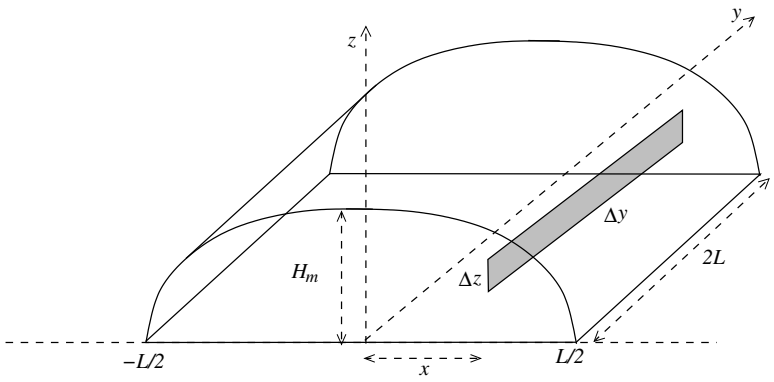

Figure 1. Shape of *gud* mound.

to derive $H(x)$. The maximum height of the *gud* mound is H_m and from the figure it is clear that $H(x=0) = H_m$. Consider the density (ρ) of the *gur* to be constant. As one may easily verify the pressure inside the *gud* mound is independent of y and at a point (x, z) can be written as [1]

$$\rho g(H(x) - z)$$

where we have neglected the atmospheric pressure.

Consider a vertical slab $\Delta y \Delta z$ (shaded area in Fig. 1) located at x and in equilibrium. Because of the x to $-x$ symmetry (about the yz plane), we will consider only the $x > 0$ side. The horizontal force is in $+x$ direction exerted on the slab due to the pressure exerted by the gur mound can be calculated. A simple integration yields

$$F(x) = \Delta y \int_0^{H(x)} \rho g(H(x) - z) dz = \frac{\rho g H(x)^2}{2} \Delta y \tag{1}$$

The vertical slab $\Delta y \Delta z$ is subjected to two forces, one from the centre side (x) and the other from the peripheral side ($x + \Delta x$). Thus the net horizontal force on the slab is

$$\Delta F = F(x) - F(x + \Delta x) = -\rho g H(x) \frac{dH}{dx} \Delta x \Delta y \tag{2}$$

Now the slab is in equilibrium. We note that the jaggery is in a hot semi-solid viscous state akin to coal tar. Thus there is a shearing stress on the *gud* slab (σ_g) which opposes the net force derived above. This viscous force is $\sigma_g \Delta x \Delta y$ which yields

$$\begin{aligned} \sigma_g &= -\rho g H(x) \frac{dH}{dx} \\ &= -\frac{\rho g}{2} \frac{d}{dx} H(x)^2 \end{aligned} \tag{3}$$

The sign is negative since $H(x)$ is a decreasing function of x. We can solve Eq. (3) with the boundary condition $H(L/2) = 0$ to obtain the dependence of height on coordinate x. Note that you are looking at the $x > 0$ side. For the $x < 0$ side

$$H(x) = \sqrt{\frac{\sigma_g L}{\rho g}\left(1 - \frac{2x}{L}\right)}$$

and the maximum height by inserting $x = 0$ in the above equation. Thus

$$H_m = \sqrt{\frac{\sigma_g L}{\rho g}} \tag{4}$$

The total volume (V) of the (*gur*) mound can be calculated by integrating Eq. (5) and multiplying by the constant factor along the y-axis, namely $2L$. Keeping in mind the symmetry of the mound on either side of the yz plane yields an additional factor of two.

$$\begin{aligned} V &= 4L \int_0^{L/2} H(x)dx \\ &= 4L\sqrt{\frac{\sigma_g L}{\rho g}} \int_0^{L/2} \sqrt{1 - \frac{2x}{L}}dx \\ &= \frac{4}{3}L^{5/2}\sqrt{\frac{\sigma_g}{\rho g}} = \frac{4}{3}L^2 H_m \end{aligned} \tag{5}$$

3. DISCUSSION

The Equation (4) for the maximum height could also be derived by dimensional analysis. The shape of viscous fluids is determined by two opposing forces: gravity and the force of viscosity and/or surface tension. In the current case we are in the happy situation that the dimensionless factor is unity, hence the dimensional analysis yields the exact result.

The base area $A \simeq L^2$, so the volume as evidenced in Eq. (5) scales as $V \simeq A^{5/4}$. This scaling relation for the spread of a viscous fluid is perhaps general. For a viscous system with given density and shear stress it is a consequence of the fact that the height decreases parabolically with the spread along the x direction.

A related question is why the shape of the mound remains invariant as the semi-solid jaggery is poured periodically and gently over a span of several hours. This appears to be a case of self-organized criticality (SOC). Additionally the shapes of several viscous substances may also be susceptible to similar analysis. We plan to examine these issues in detail in the future.

The density of the jaggery *gur* found in our house hold is around 1300 kg/m^3 [2]. Taking $L = 4$ m and $H_m = 1$ m, the total mass of a gur mound will be roughly equal to 28 tonnes. This gives $\sigma_g \approx 3.25$ kPa. We urge the reader to buy jaggery, verify our model and experiment further. Physics is sweet, physics is fun!

4. ACKNOWLEDGMENTS

One of us (LPSK) gratefully acknowledges discussions with B. S. Sharma and Dr. H. S. Vashistha of his school. PP acknowledges the support of National Initiative on Undergraduate Sciences (NIUS) programme undertaken by the Homi Bhabha Centre for Science Education (HBCSE-TIFR), Mumbai, India and some unpublished notes of Siddharth Singh on hydrodynamics.

References

[1] Halliday D., Resnick R., and Walker J. 1994 *Fundamentals of Physics* (New Delhi: Asian Books Pvt. Ltd.)

[2] Supriya D Patil and S V Anekar, 2014, "Effect of Different Parameters and Storage Conditions on Liquid Jaggery Without Adding Preservatives", Intnl J of Res in Engg and Tech, **12**, 280 - 283

Unfolding Proteins: Fast versus Slow

T. Saxton[1*], J. Slivka[2] and M. J. Comstock[3]

[1] Third year, B. Sc, Department of Physics, Illinois State University, Normal, Illinois

[2] Second year, B.S. Department of Physics and Astronomy, Michigan State University, East Lansing, Michigan

[3] Department of Physics and Astronomy, Michigan State University, East Lansing, Michigan

*Email: tasaxt1@ilstu.edu

Abstract:

As the structure of the protein is essential to its function, a better understanding of protein folding is fundamental to understanding protein function. [1] This comprehension of the function and folding of proteins will enable medicine to synthesize proteins in a way currently not possible. One of the major hurdles is that the protein has the capability of folding in different ways and speeds. The goal of our experiment is the examination of the hYAP protein, and to see the different speeds of folding that it undergoes. Our specific goal was to find instances of fast folding of the protein - folding occurring within less than a millisecond. The methodology behind this experimentation is presented, along with results for fast folding of the protein, and slow folding of the protein.

1. INTRODUCTION

Current engineering of proteins is difficult, because of the direct relationship of function and folding. Furthermore, a greater understanding of protein folding can provide a possible method of combating prions - proteins that have folded in a manner different than their native structure. At times a function detrimental in comparison to the standard function will arise as a result of this abnormal folding. This abnormal folding can result in other proteins folding abnormally as well, leading to diseases such as bovine spongiform encephalopathy in certain animals, Creutzfeldt-Jakob disease, Alzheimer's disease or Gerstmann-Straussler syndrome in humans for example. [2] [3] By understanding how proteins fold, the possibilities of chemical synthesis of proteins for individuals with unique dietary needs becomes possible. [4] Consequently, a greater understanding of diseases thought to be caused by prions will lead towards more efficient treatment of these diseases. In this paper, we use the single molecule trapping technique to study protein folding. This technique is useful in this matter as it allows us to build a stochastic model of the protein, one molecule at a time. This is in contrast to other methods that result in building a model of the protein that is an average of the behavior. In this experiment, we utilize an optical trapping method in which we capture two "beads" that when placed in the optical traps form a DNA tether with each other.

2. EXPERIMENTAL

2.1 Overview of Trapping Method

The sample chamber and experimental set up is contained in a room of its own, with baffling on the walls to prevent noise pollution, and the lights off to prevent light pollution from affecting the experiment. With the beads captured in the optical trap, the motion of the beads can be controlled to a certain degree. The trap itself is conical in shape and creates a restoring force upon the bead trapped within it. If the trap is moved to the left, the bead will be pulled to the left as well as it re-centers itself in the trap. This is what allows us to directly apply a force to an individual protein. A calibration is found for every bead pair that tells us the trap stiffness and the conversion constant for determining the position of the beads. Once this is done, the beads begin fishing for a tether. This entails one of the optical traps remaining stationary, while the other oscillates closer and further from the stationary optical trap. The streptavidin beads have a DNA strand on them, followed by the protein, followed by another strand of DNA. The strand of DNA not directly on the streptavidin bead forms a digoxygenin with anti-digoxygenin bond with the anti-digoxygenin bead. The successful formation of this bond is what is called a tether. Once a peak force is measured during the movement further from the stationary trap, this is indicative that the DNA from the streptavidin bead has formed a tether with the anti-digoxygenin bead. At this point, the bead pair is able to be used to exert force on the protein such that it will unfold, as seen in Figure 1.

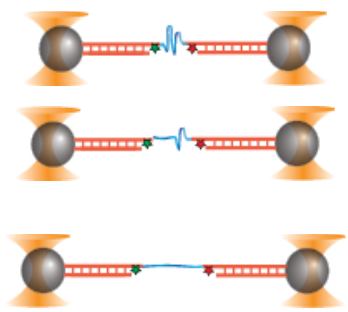

Figure 1: Starting from the top, the beads are tethered together by the DNA. Left to right, it is an anti-digoxygenin bead, DNA, the protein under examination, DNA, and finally the streptavidin bead. As the beads are moved further apart, the protein experiences a force and eventually unfolds.

The beads are caught in the optical trap by the platform the sample chamber is mounted on being moved. This movement is controlled outside of the room the sample chamber is contained in.

2.2 Optical Trap Set-up

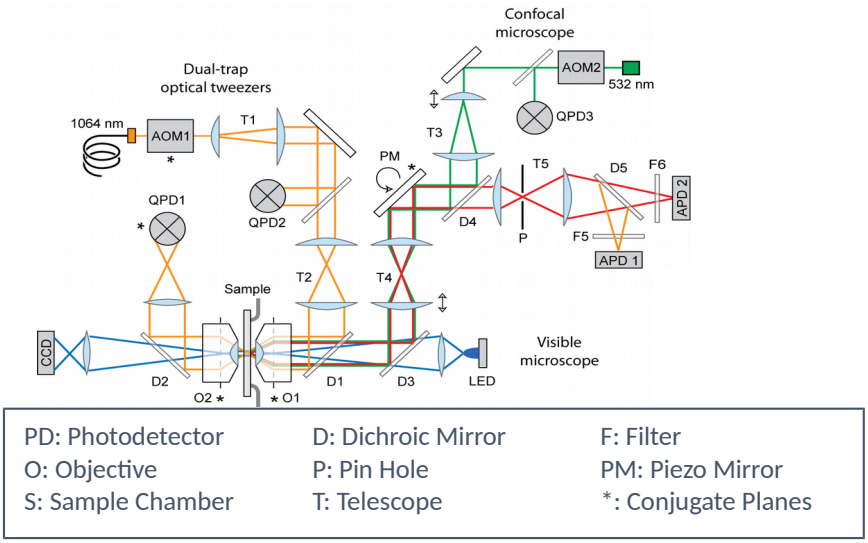

Figure 2: The experimental setup. [5]

The laser used in this experiment is in the infrared spectrum at 1064 nm and is a 5W laser. One of the objectives is held fixed, while the other is allowed to be moved perpendicularly towards and away from the sample chamber (see figure 2). This movement changes the diameter of the laser beam, and provides better collimation of the laser. The accuracy of the collimation is checked with the aid of an infrared fluorescent card. The camera focused on the experiment has two lenses in front of it, an ultraviolet lens and an infrared lens. When the infrared lens is filtering light, the laser can be seen on a monitor. This allows a visual check of the laser to be conducted. The experimentalist looks for a shape that is as near a uniform circle as can be obtained visually. If the circle appears to be more elliptical, this is indicative that the sample chamber itself is not presenting a vertical surface for the laser to pass through, and as such the laser is coming out angled rather than straight. This is adjusted by physically rotating the chamber to achieve a uniform circle rather than an ellipse. This is a measure taken to ensure that before the sample is being experimented with, the optical trap will successfully capture the beads. If the chamber is not presenting a vertical surface for the laser to pass through, this can lead to issues during the experiment. As the sample chamber is moved, the angling can result in the captured bead being removed from the optical trap. This occurs because if the sample chamber is angled, as it is moved the odds of the optical trap causing a bead to collide with the surface of the sample chamber increase.

2.3 Preparation of Sample Chamber

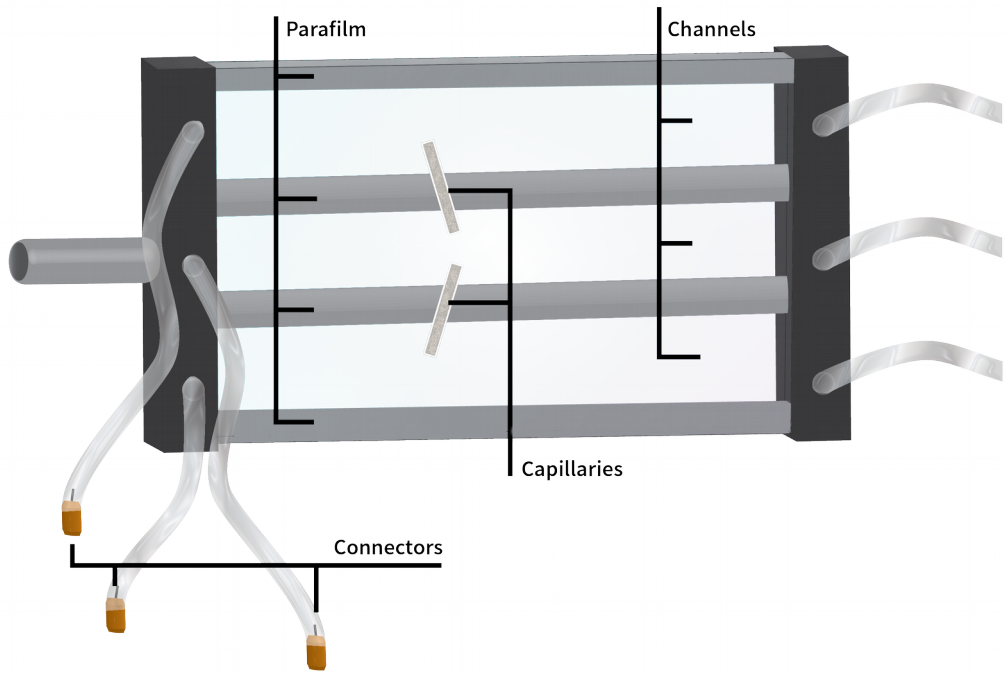

Figure 3: The sample chamber. Syringes are connected to the connectors, which have a needle on them attaching them to a tube. Through these tubes, the buffer, streptavidin and anti-digoxygenin beads flow through the channels. The capillaries allow the beads in the top and bottom channels to flow into the middle channel where the optical trap is then used to capture the beads and perform the experiment. The fluids then leave the chamber through the tubes on the left. Image is not to scale. Image credit: Fallyn Stieglitz

Before the experiment can be conducted, the sample chamber must be prepared for the optical trap. The chamber used in this experiment is constructed out of cover glass and parafilm (see figure 3). The parafilm is used to create three separate channels on the cover glass: the bottom channel is where the streptavidin beads with the protein construct flow through, the middle channel is where the buffer solution flows through, and the top channel is where the anti-digoxygenin beads flow through. On the middle channel there are two capillaries connecting the channel to the top and bottom channels. These capillaries are what allow the beads to flow through to the middle channel and be captured by the optical trap. The chamber is initially prepared for a trapping session by first pushing milli-Q water (filtered 0.2 microns) through the channels using syringes. This is done to ensure that no excess of experimental materials is wasted. The purpose of pushing the milli-Q through the channels is to ensure that there are no air bubbles covering, or in, the capillaries before the experimental materials are added. The beads are

on the order of a micron in size and would not be able to flow into or through the capillary if an air bubble is blocking the capillary in any way. The chamber is then placed between the objectives of the experimental setup and visually verified for the clear openings on the capillaries by the experimentalist. These syringes containing the milli-Q are left connected to the sample chamber until the syringes containing the sample to be used are connected to the chamber. This is another step taken to ensure that no air gets into the chamber and causes bubbles that might interfere with a capillary.

2.4 Sample Preparation

The preparation of the sample involves making the buffer solution. The buffer solution is a combination of Triss-HCl, Glucose, NaCl, and water in a centrifuge tube. Three separate centrifuge tubes are then used to portion out the buffer solution. After the buffer has been portioned, the beads are then added to the tubes. Before adding the anti-digoxygenin beads to a tube, the beads are first vortexed. This is to ensure that upon pipetting the beads, the container has a uniform concentration of beads as over time the beads will settle at the bottom of the container. The streptavidin beads are then added to a separate tube, after being mixed by inverting or flicking the container. As the streptavidin beads have DNA attached to them, they cannot be vortexed as this would shred the DNA. Finally, pyranose oxidase (poxy) is added to all three tubes. The purpose of the addition of the poxy is to prevent oxygen from interacting with the solution as best as possible. Oxygen in solution can get converted into “radical oxygen”. Radical oxygen is highly reactive and will react with the molecules, possibly breaking the DNA tethers or damaging the protein under study. The poxy is an oxygen scavenger, and will keep the radical oxygen from reacting within the solution. The three separate mixtures are then transferred into separate airtight syringes. The airtight syringes and the poxy are implementations put into place to mitigate waste of material and ensure that oxygen is not a reason for lack of success during the experiment. However, at some point the poxy will become saturated with oxygen, and unable to scavenge any more oxygen from the solution. This will typically end the experiment, as the oxygen will now be able to interact with the DNA and prevent tethers from being formed successfully. To begin the experiment, the airtight syringes replace the syringes currently attached to the sample chamber. During this replacement, it is imperative that air not be able to enter the tubes of the sample chamber. To prevent this, the experimentalist adds milli-Q to the connection location, to ensure that once the airtight syringe is connected, there is no air between the solution contained within the syringe and the milli-Q currently in the tubes of the sample chamber. The airtight syringes are then placed in specific positions that correspond to controls used by the setup to control the flow of the beads (anti-dixoxygenin or streptavidin) and the buffer. There are

motorized syringe pumps at these positions that push the solution out of the syringes at speeds ranging in the hundreds of nanoliters per second.

2.5 Application of Force to Protein Construct

Once this is done, the goal is to trap an anti-digoxygenin bead in one optical trap, a streptavidin bead in the other optical trap, and then form a tether between the two beads using the DNA. Once the beads are both successfully caught in the optical trap, a calibration of the trap for this bead pair is done. This will determine the trap stiffness constant and a conversion constant that gives the bead position from the optical method. [5] The calibration also gives the experimentalist a control over data collection. For bead pairs of a sample protein, the calibration for a bead pair should not be vastly different in comparison to other bead pairs of the same sample protein. If a bead pair presents a calibration that is outside of the standard calibration for a sample protein, it is immediately apparent to the experimentalist that this bead pair cannot be used for data collection. This can happen for a variety of reasons: the beads vary in size, there could be more than one bead in the optical trap, there could be multiple tethers formed between the beads, the sample protein could possibly be bad. If the calibration is within the standard calibration for the sample, the beads then form the tether. Once the tether has been formed, a force can be applied to the protein. This is done quickly at first, to test whether or not the tether is stable. One of the optical traps is held stationary, and the other trap moves away from it (see figure 1) which cause the force to be applied to the protein. At a certain force the protein will unfold, and this force is measurable. After this fast scan has been performed, a slow scan is performed. The slow scan involves the trap moving in discrete jumps as it moves away from the stationary trap. The slow scan is performed in order to see the fast folding occur. The fast folding occurs rapidly, in times less than a millisecond; scanning too quickly risks missing these fast folding occurrences. By scanning slowly, we keep the protein at a certain force for a longer time. Due to the statistical mechanical nature of folding, at certain forces the unfolded state will be just as likely to occur as the folded state. This slow scan allows us to see this happen, as shown in the following results.

3. RESULTS AND DISCUSSION

3.1 Slow Folding Proteins

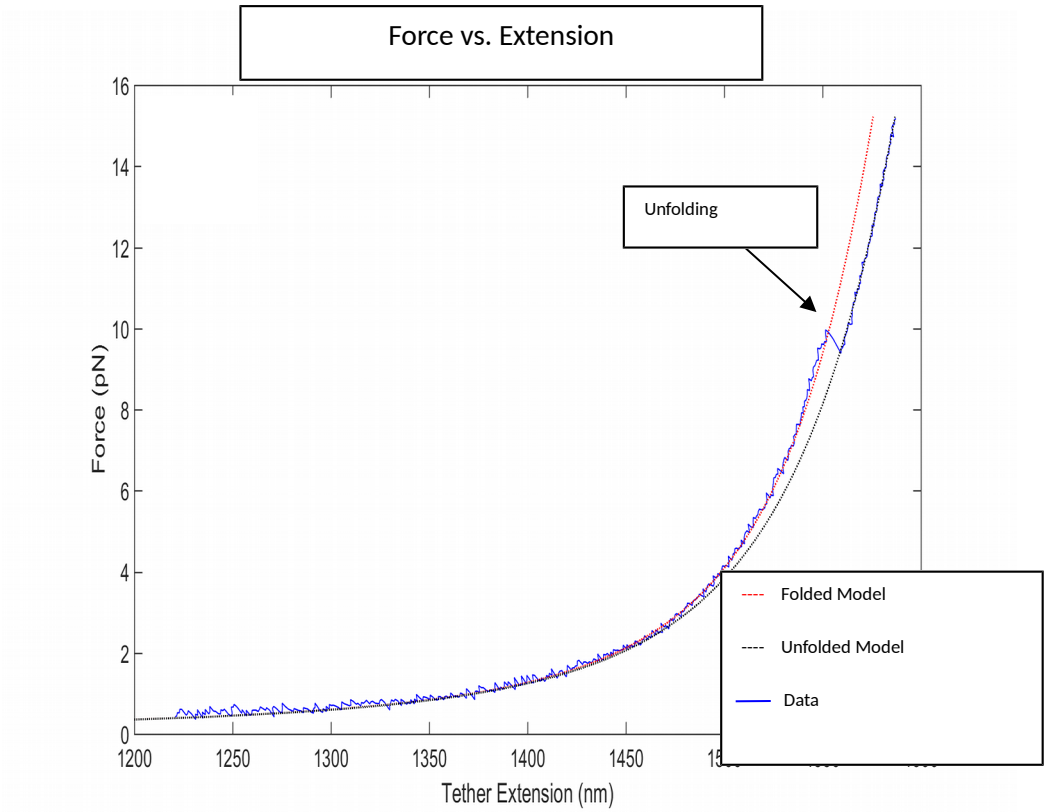

Figure 4: An example of slow folding. In comparison to fast folding, slow folding takes place in half to full seconds.

Shown in figure 4 is an example of slow folding. There are two different models to describe the dependence of the tether extension on the force applied: a model for the protein folded, and a model for the protein unfolded. The molecules are modelled using the statistical mechanics of polymers. One of these models includes the unfolded protein polymer, the other does not. At low forces, the models are indistinguishable from one another, but as the force increases, the models separate. This separation between models is used to identify when and where the protein unfolds. In the example presented, the protein extended slightly less than 1550 nm, at which point the protein then unfolded (indicated by the arrow), at a force of approximately 10 pN. The data is interpreted as a representation of slow folding because as can be seen at the point of unfolding, there is a single distinct jump; the blue line moves from the folded model to

the unfolded model and stays there.

3.2 Fast Folding Proteins

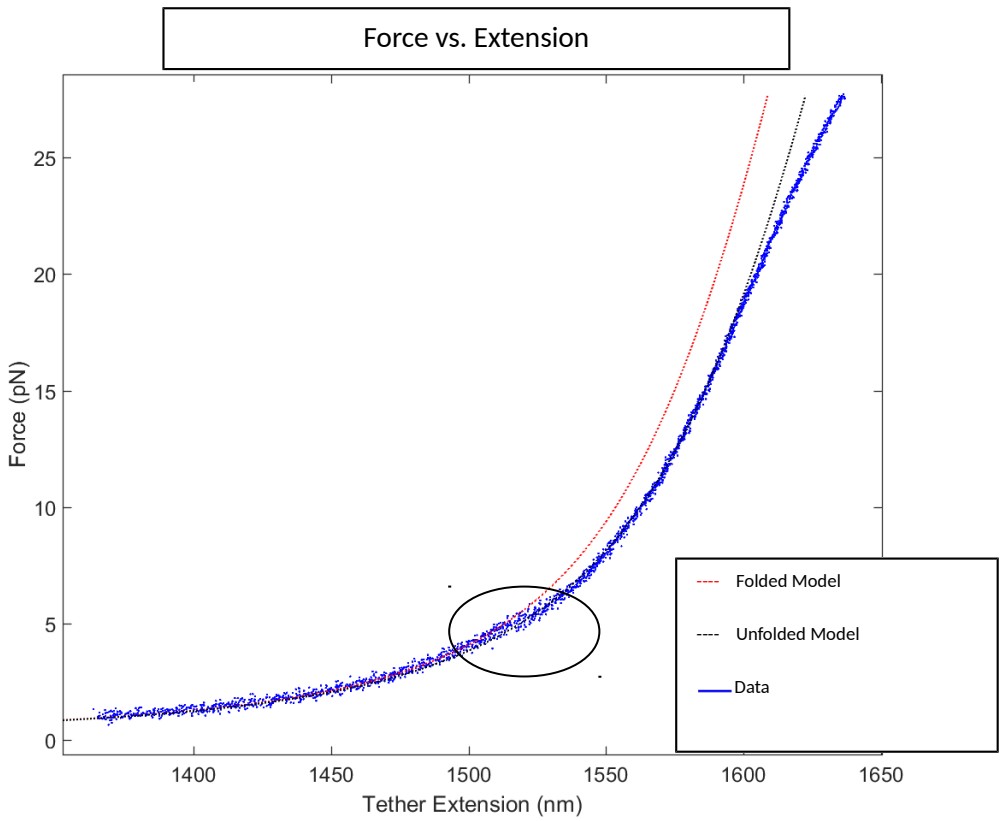

Figure 5: An example of fast folding. The expected time for fast folding to occur is in the millisecond time range. As seen in the circled area, the data is not just following one model. The data points, if followed sequentially, would alternate between the folded model and the unfolded model as the protein switches between the two states rapidly.

Shown in figure 5 is an example of fast folding. The difference here being that rather than there being a single distinct jump, there is more of a smooth transition between the folded and unfolded models that occurs over an extension range. This is due to how the data is taken; as the data is being taken, it is being averaged to avoid files of an excessive data size. The above is said to be fast folding because it is not folding just once, but jumping between models rapidly. The result is that as the protein is jumping between the models, at the lower force it spends a greater amount of time folded than it does unfolded. As the force increases, the time spent folded lessens and it is more likely

to find the protein in an unfolded state, until finally the protein is unfolded and following the unfolded model.

3.3 Conclusion

Based upon the data taken during these experiments it was determined that fast folding was possible for the protein construct. However, these instances of this different folding were few and far between. Over the course of 8 weeks of experimentation, we found 4 instances that were believed to be indicative of fast folding. However, we have shown that the methodology presented is useful for examining different folding procedures for a given protein. As a result of this, future studies will be made involving a protein construct Protein G, as it has also shown possibilities of there being different types of folding occurring. Whereas before it seemed to have two distinct states, the folded and unfolded state, through the use of this method there is evidence to suggest that there might be a state in between the folded and unfolded states. This in between state of Protein G is the focus of future studies using this method.

ACKNOWLEDGEMENTS

T.S. and J.S. would like to acknowledge the Comstock Laboratory and Dr. Matthew Comstock for his mentorship at Michigan State University. T.S. received support from a Research Experience for Undergraduates (REU) supported by the NSF (1559776). The work was also supported by a grant from the NSF to the Comstock lab (MCB-1514706).

REFERENCES

[1] Collinge, J. (2001). Prion diseases of humans and animals: their causes and molecular basis. London, England.

[2] Hartl, U. (2010). Protein Folding: mechanisms and role in disease.

[3] James A. Olzmann, K. B.-S. (2003, December 9). Familial Parkinson's Disease-associated L166P Mutation Disrupts DJ-1 Protein Folding and Function. Atlanta, Georgia, United States of America.

[4] Nilsson, B. L., Soellner, M. B., & Raines, R. T. (2005). Chemical Synthesis of Proteins. *Annual Review of Biophysics and Biomolecular Structure*, *34*, 91–118. http://doi.org/10.1146/annurev.biophys.34.040204.144700

[5] Comstock, M. J., Ha, T., & Chemla, Y. R. (2011). Ultrahigh-resolution optical trap with single-fluorophore sensitivity. *Nature Methods*, *8*(4), 335-340. DOI: 10.1038/nmeth.1574

STUDENT JOURNAL OF PHYSICS

Study of low energy proton capture resonances in ^{14}N

Rajan Paul[1], Sathi Sharma[2], Sangeeta Das[2], M. Saha Sarkar[2*]

[1]Second year, M.Sc., Department of Physics, VIT University, Vellore-632014, India
[2]Nuclear Physics Division, Saha Institute of Nuclear Physics, Kolkata-700064, India
[*]maitreyee.sahasarkar@saha.ac.in

Abstract: Several proton capture resonances in ^{14}N have been studied theoretically using partial wave analysis technique. Most of the results agree well with available experimental data. The analysis has been extended to indicate that one of the resonances with uncertain spin may need a change in the assignment.

1. INTRODUCTION

Study of radiative low energy proton capture reactions has several important implications in nuclear astrophysics. Experimental data on the capture cross sections at stellar energies are essential for studying primordial nucleosynthesis. The measurements at stellar energies are difficult as the direct capture cross-sections are very low. Usually data measured at higher energies are extrapolated to lower energies, which may fail if there are low energy resonances. The astrophysical capture reaction rate is thus greatly affected by the capture resonances at the stellar energies.

The partial wave analysis technique for studying nuclear radiative capture resonances is well-established. This analysis is also useful to search for new resonances and to predict their quantum numbers. In the present work, various experimentally observed resonances [1] in ^{14}N are reproduced reasonably well using this theory. Spectroscopic factors for these states have also been estimated. Some of the deviations of the theoretical results from data are discussed for future scopes.

2. THEORETICAL APPROACH

2.1. The Code

The code **wspot** [2] has been utilized for the partial wave analysis. This program utilizes Woods-Saxon potential as the phenomenological one-body potential. It provides well-accepted results for the properties of bound-state and continuum single-particle wavefunctions. The parameters of the potential are chosen to have a best fit of nuclear single-particle energies and nuclear radii. This potential is composed of the sum of a spin-independent central potential, a spin-orbit potential, and the Coulomb potential. The code thus provides single-particle energies and single-particle radial wavefunctions for the bound states of Woods-Saxon potential with quantum numbers n_r, l and j. It also calculates the nucleon scattering cross-sections for given l and j values.

2.2. The Parameters

The set of parameters used for the Woods-Saxon potential are V_0 (central part)= −53 MeV, V_1 (central part – isospin dependent= −30 MeV and V_{so} (spin-orbit)= 22 MeV for the potential strengths, and r_o (radius parameter–central) = r_{so} (radius parameter–spin-orbit) = 1.25 fm and a_o (diffuseness–central)= a_{so} (diffuseness – spin-orbit)= 0.65 fm for geometry. The radius for the Coulomb term is smaller with r_c = 1.20 fm.

2.3. Determination of phase shifts

The code **wspot** [2] is used to calculate the energies and widths of the capture resonance states [1]. An incident particle is captured to form a metastable bound state which subsequently decays by emission of gamma or by release of a particle. For a given (l, j) value the program calculates the phase shift $\delta(E)$ and the scattering cross section $\sigma(E)$ as a function of energy. The cross-section can be expressed as:

$$\sigma_{\text{total}} = \frac{4\pi}{k^2} \sum_{l=0}^{l_{\max}} (2l+1) \sin^2 \delta_l$$

2.4. Determination of energies of resonant levels and their widths

By varying the energy of the incoming particle the relative phase of the inner and outer wavefunctions are changed. The energy E_0 where the amplitude of inside and outside wavefunctions match, cross-section has maximum value. This energy E_0 is known as a resonance energy. Only one partial wave 'l' is necessary to have the occurrence of a

resonance state corresponding to the energy E_0 where $\Gamma_l = \Gamma/2$. The width of the resonance (Γ) is determined from the energy (E), where cross-section reduces to half of a central value $(E-E_0) = \pm\Gamma/2$.

E_x (MeV)	E_R (MeV)		V_N factor	Width (Γ) (keV)		Spectro-scopic Factor ($\Gamma^{expt}/\Gamma^{theo}$)	Single Particle Orbital
	Expt [1]	Theo		Expt [1]	Theo		
7.966 (2^-)	0.416	0.411	0.933	<0.37	0.212	1.74	$1d_{5/2}$ (l=2)
8.062 (1^-)	0.512	0.515	0.972	23 (1)	66.8	0.34	$2s_{1/2}$ (l=0)
8.620 (0^+)	1.07	1.07	0.703	3.8 (3)	124	0.03	$1p_{1/2}$ (l=1)
8.776 (0^-)	1.226	1.074	0.914	410 (20)	475	0.86	$2s_{1/2}$ (l=0)

Table 1: Comparison of experimental and theoretical features of the low energy resonance states at different excitation energies (E_x) in ^{14}N.

2.5. Inputs needed to identify a resonance

The energy range that could be populated in the compound nucleus by capture of the incoming projectile by the target nucleus is determined by the energy given in the input and the Q value of the reaction. The incoming particle energy necessary to populate a resonant state is known as resonance energy (E_r).

The resonances which are already identified in a particular nucleus can be reproduced to get an idea of the spectroscopic purity of the state. For a particular choice of l and j, the depth of the central potential is varied (normalized) by a factor such that the resonance energy is determined correctly. The ratio of widths of the resonance obtained in experiment over theory provides a measure of the spectroscopic factor of that particular state.

By fixing a particular depth of the potential as estimated from reproducing known resonances – unknown resonances can be also identified which corresponds to a specific single particle orbit (l,j).

3. RESULTS AND DISCUSSION

3.1. Study of known proton capture resonances in ^{14}N

The Q value for the reaction $^{13}C+p\rightarrow{}^{14}N+\gamma$ is 7550 keV. The ground state spin of ^{13}C is $1/2^-$. The known resonances [1] have been reproduced by varying the potential depths. The single particle orbits are chosen keeping in mind the spin assignment in ^{14}N, as well as the earlier information of the l value. The results are shown in Figure 1 and Table 1. Figure 1 shows the features of different resonances in ^{14}N. In Fig 1a, the variation of the normalization factor of the potential to choose the best value for reproducing the experimental resonance energy is demonstrated for a particular case. In Fig 1b, the resonance at 8062 keV (1^-), reported to be originated from l=0, has been shown to be reproduced by the l=2 contribution. However in Table 1, the spectroscopic factor has been calculated for l=0 contribution only. Figs 1c and d show the features for other resonances.

The results show quite good agreement with the experimental data. However, except for the 0- state at 8776 keV, the spectroscopic factors for the other states do not appear to be realistic. The normalization factors for the potential corresponding to different shells and l values are consistent. For $d_{5/2}$ and $s_{1/2}$ orbitals, the normalization is less than 1 (~0.91-0.97), whereas for $p_{1/2}$, it needs 30% reduction (~0.7), indicating that the resonance energies are under predicted with full strength of the potential. However, in Fig.1 b, while reproducing the resonance (1^-) with $d_{3/2}$, the resonance energy is over predicted resulting in a normalization value > 1 (~1.35).

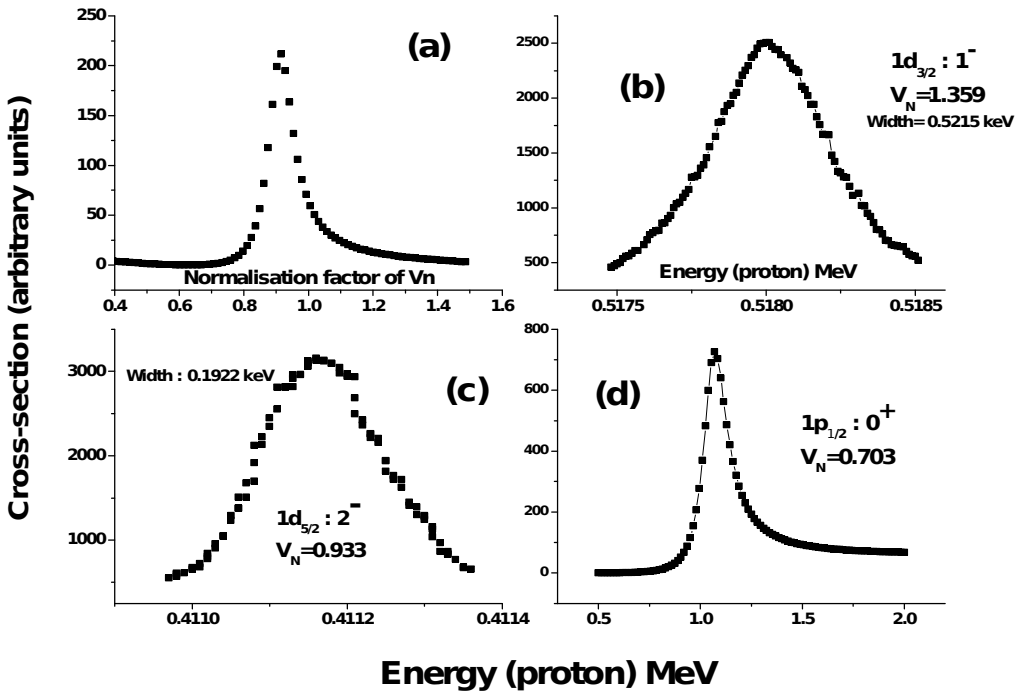

Figure 1: Theoretical results for different resonances. See text for details.

3.2. Comments on resonance states with relatively higher spins

In the present work, no excitation of the target has been considered. With this assumption, having a resonance with spin >3 (4) with negative (positive) parity at low energies (E_r< 1000 keV) is unlikely as those will need coupling with l=4 (5) partial wave, i.e *g* (*h*) orbitals. However, such states have been reported in literature [1].

Thereafter, with normalization around 0.91 as obtained for $d_{5/2}$ for known resonances, the energies are varied and a resonance is obtained at E_R~0.8 MeV (Fig. 2). The energy almost matches with an observed state at 8490 keV with a tentatively assigned spin of (4^-). However, having two close-by resonances with same l is also doubtful. This spin assignment therefore needs to be revalidated experimentally.

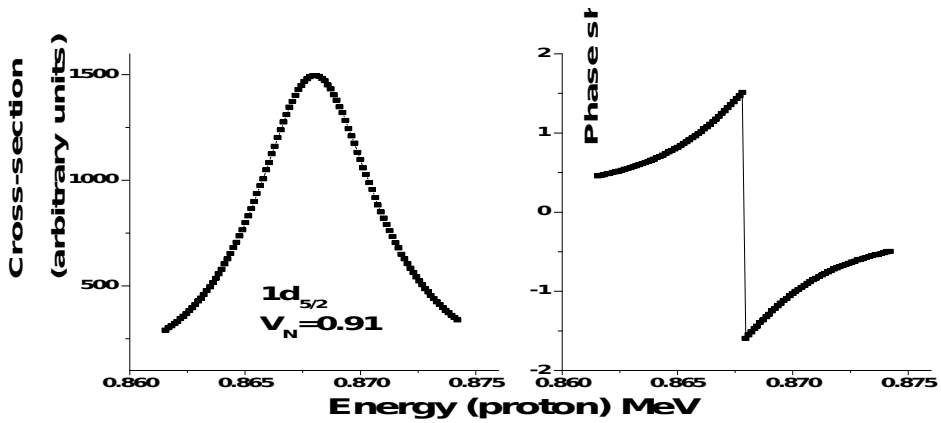

Figure 2: The resonance at E_r~0.866 MeV

4. CONCLUSION

Several proton capture resonances in ^{14}N have been studied theoretically using partial wave analysis technique. Most of the results agree well with available experimental data. The spectroscopic factors are determined. The analysis has been extended to indicate that one of the resonances with uncertain spin may need a change in the assignment.

5. ACKNOWLEDGEMENTS

The authors are thankful to Prof. Sukhendusekhar Sarkar, Department of Physics, IIEST Shibpur for fruitful discussions.

References

[1] www.nndc.bnl.gov; F. Ajzenberg-selove, *Nucl. Phys. A* **523**, 1 (1991)**.**

[2] B. A. Brown, (WSPOT code), http://www.nscl.msu.edu/~brown/reaction-codes/home.html

STUDENT JOURNAL OF PHYSICS

Volume 6 **Number 3** **Jul - Sep 2017**

CONTENTS

ARTICLES